HHS Public Access

Author manuscript

JACC Cardiovasc Imaging. Author manuscript; available in PMC 2017 September 08.

Published in final edited form as:

JACC Cardiovasc Imaging. 2016 August ; 9(8): 950–961. doi:10.1016/j.jcmg.2016.01.020.

In vivo PET imaging of high-density lipoprotein in multiple atherosclerosis models

Carlos Pérez-Medina, PhD[*], **Tina Binderup, PhD**[†], **Mark E. Lobatto, MD, PhD**[‡], **Jun Tang, PhD**[§], **Claudia Calcagno, MD, PhD**[*], **Luuk Giesen, BSc**[*], **Chang Ho Wessel, MD**[*], **Julia Witjes, MD**[*], **Seigo Ishino, PhD**[*], **Samantha Baxter, MHS**[*], **Yiming Zhao, PhD**[*], **Sarayu Ramachandran, PhD**[*], **Mootaz Eldib, MSc**[*], **Brenda L. Sánchez-Gaytán, PhD**[*], **Phillip M. Robson, PhD**[*], **Jason Bini, PhD**[‖], **Juan F. Granada, MD**[¶], **Kenneth M. Fish, PhD**[#], **Erik S.G. Stroes, MD, PhD**[‡], **Raphaël Duivenvoorden, MD, PhD**[‡], **Sotirios Tsimikas, MD**[††], **Jason S. Lewis, PhD**[§], **Thomas Reiner, PhD**[§], **Valentín Fuster, MD, PhD**[‡‡], **Andreas Kjær, MD, PhD**[¶¶], **Edward A. Fisher, MD, PhD**[##], **Zahi A. Fayad, PhD**[*], and **Willem J.M. Mulder, PhD**[*,‡]

[*]Translational and Molecular Imaging Institute, Icahn School of Medicine at Mount Sinai, New York, NY, USA [†]Clinical Physiology, Nuclear Medicine, PET and Cluster for Molecular Imaging, University of Copenhagen, Denmark [‡]Department of Vascular Medicine, Academic Medical Center, Amsterdam, The Netherlands [§]Department of Radiology, Memorial Sloan Kettering Cancer Center, New York, NY, USA [‖]School of Engineering & Applied Science, Yale University, New Haven, CT, USA [¶]CRF-Skirball Center for Innovation, The Cardiovascular Research Foundation, Orangeburg, NY, USA [#]Cardiovascular Research Center, Icahn School of Medicine at Mount Sinai, New York, NY, USA [††]Division of Cardiovascular Diseases, Department of Medicine, University of California San Diego, La Jolla, CA, USA [‡‡]Zena and Michael A. Wiener Cardiovascular Institute, Icahn School of Medicine at Mount Sinai, New York, NY, USA [¶¶]Clinical Physiology, Nuclear Medicine and PET, University of Copenhagen, Denmark [##]Leon H. Charney Division of Cardiology and Marc and Ruti Bell Program in Vascular Biology, New York University School of Medicine, New York, NY, USA

Abstract

Objectives—Our aim was to develop and validate a non-invasive imaging tool to visualize HDL's *in vivo* behavior by positron emission tomography (PET), with an emphasis on its plaque targeting abilities.

Background—High-density lipoprotein (HDL) is a natural nanoparticle that interacts with atherosclerotic plaque macrophages to facilitate reverse cholesterol transport. HDL-cholesterol

Address for correspondence, Willem J.M. Mulder, One Gustave L. Levy Place, Box 1234, Tlf. 212-824-8910; Fax: 646-537-9589, willem.mulder@mssm.edu, New York, NY 10029.

The authors declare no competing financial interest.

concentration in blood is inversely associated with risk of coronary heart disease and remains one of the strongest independent predictors of incident cardiovascular events.

Methods—Discoidal HDL nanoparticles were prepared by reconstitution of its components apolipoprotein A-I (APOA1) and the phospholipid DMPC. For radiolabeling with Zirconium-89 (^{89}Zr), the chelator DFO was introduced by conjugation to APOA1 or as a phospholipid-chelator (DSPE-DFO). Radiolabeled HDL's biodistribution and plaque targeting was studied in established murine, rabbit and porcine atherosclerosis models by PET combined with computed tomography (PET/CT) or with magnetic resonance imaging (PET/MRI). *Ex vivo* validation was conducted by radioactivity counting, autoradiography and near infrared fluorescence imaging. Flow cytometric assessment of cellular specificity in different tissues was performed in the murine model.

Results—We observed distinct pharmacokinetic profiles for the two ^{89}Zr-HDL nanoparticles. Both APOA1- and phospholipid-labeled HDL mainly accumulated in kidneys, liver and spleen with some marked quantitative differences in radioactivity uptake values. Radioactivity concentrations in rabbit atherosclerotic aortas were 3–4-fold higher than in controls at 5 days p.i. for both ^{89}Zr-HDL nanoparticles. In the porcine model, we observed increased accumulation of radioactivity in lesions by *in vivo* PET imaging. Irrespective of the radiolabel's location we found HDL nanoparticles to preferentially target plaque macrophages and monocytes.

Conclusions—^{89}Zr labeling of HDL allows studying its *in vivo* behavior by non-invasive PET imaging, including visualization of its accumulation in advanced atherosclerotic lesions. The different labeling strategies provide insight on the pharmacokinetics and biodistribution of HDL's main components, *i.e.* phospholipids and APOA1.

Graphical abstract

Keywords

high-density lipoprotein; atherosclerosis; PET/CT; PET/MRI; Zirconium-89

INTRODUCTION

Atherosclerosis is a systemic inflammatory disorder that underlies cardiovascular disease (1). Lipid deposition and immune cell infiltration drive atherosclerotic plaque development

(2), which can eventually rupture (3), potentially causing atherothrombosis and ensuing acute coronary events (4).

High density lipoprotein (HDL) is a natural nanoparticle mainly composed of phospholipids, cholesterol and cholesteryl esters, and apolipoprotein A-I (APOA1), which is involved in the process of reverse cholesterol transport (5). HDL and APOA1 have demonstrated atheroprotective properties (6)(7)(8). The principal mechanism whereby HDL exerts this protective effect is generally ascribed to promoting cholesterol efflux from macrophages in plaques and transporting it to the liver for excretion, although other anti-atherogenic properties have been reported (9). Cholesterol efflux is mediated by several membrane receptors abundantly expressed on macrophages to which APOA1 and HDL bind (10)(11).

The study of HDL can be modernized by the integration of non-invasive imaging. Capitalizing on this, our group pioneered the use of HDL magnetic resonance imaging (MRI)(12)(13). However, in order to non-invasively study the pharmacokinetics, trafficking and metabolism of HDL a quantitative and highly sensitive modality is warranted. Recent advances in labeling technology now allow positron emission tomography (PET) radiotracer imaging at unprecedented high sensitivity down to the picomolar range, at limitless tissue penetration, in a so-called hot spot fashion (14). Tracing of HDL requires long-lived radioisotopes as, upon intravenous administration, it circulates for extended periods of time. Recently, we have developed modular Zirconium-89 (^{89}Zr)-labeling methods for lipid-based nanoparticles (15)(16). The physical half-life of ^{89}Zr (78.4 h) makes it an ideal radiolabel for such long-circulating materials (15), and provides an opportunity to study HDL nanoparticles' *in vivo* behavior.

Through extensive studies involving a unique set-up combining PET/CT and PET/MRI, in murine, rabbit and porcine atherosclerosis models, we demonstrate that ^{89}Zr labeling is a valuable tool to non-invasively assess pharmacokinetics and distribution of HDL's main components.

METHODS

A detailed description of the animal models and experimental procedures can be found in the supplementary information. All animal experiments were performed in accordance with protocols approved by the Institutional Animal Care and Use Committees of Mount Sinai, Memorial Sloan Kettering Cancer Center and/or CRF-Skirball Center for Innovation, and followed National Institutes of Health guidelines for animal welfare.

RESULTS

Radiolabeling of HDL nanoparticles

The composition, DLS-measured size and size exclusion retention time for all HDL nanoparticles used in this study are summarized in table S1. In order to incorporate the radioactive label (^{89}Zr), we either conjugated DFO to APOA1 via its attachment to lysine residues, or included the phospholipid chelator DSPE-DFO in the formulation of the particles. Reaction of these DFO-bearing nanoparticles with ^{89}Zr-oxalate generated ^{89}Zr-

APOA1-labeled HDL (^{89}Zr-AI-HDL, figure 1A, left) or ^{89}Zr-phospholipid-labeled HDL (^{89}Zr-PL-HDL, figure 1A, right), at high radiochemical yields (96 ± 2 [n = 5] and 81 ± 10 % [n = 7], respectively), and radiochemical purities of > 98 %. Radiolabeling did not impact HDL's size (rHDL, table S1).

Cellular targets of HDL nanoparticles

In addition, we prepared fluorescent, non-radioactive analogs of the two ^{89}Zr-labeled HDL nanoparticles to investigate their cellular targets in different tissues by flow cytometry (figures 1B and S1). These particles were prepared in identical manner to their radioactive counterparts, but contained the dye DiR (table S1) and non-radioactive Zr. In *Apoe*$^{-/-}$ mice, flow cytometric analyses revealed little targeting differences between the two Zr-labeled nanoparticles in blood, spleen and aorta at 24 h p.i. (figure 1C). In atherosclerotic aortas, macrophages and monocytes were preferentially targeted over neutrophils (4.5- and 3.1-fold greater DiR uptake, respectively) and lineage-positive cells (290- and 220-fold greater DiR uptake, respectively), whereas mostly macrophages were targeted in the spleen. In blood, dendritic cells and monocytes were targeted to nearly the same extent.

Pharmacokinetics and biodistribution of ^{89}Zr-HDL nanoparticles in mice

Blood radioactivity clearance in *Apoe*$^{-/-}$ and wild type mice was investigated (figure 2A). The weighted half-lives for ^{89}Zr-AI-HDL-associated radioactivity (figure 2A, top) in blood were 1.4 and 2.0 h in atherosclerotic and wild type mice, respectively, whereas for ^{89}Zr-PL-HDL (figure 2A, bottom) these values were 2.8 and 1.1 h. Radioactivity distribution at 24 and 48 h was also measured for selected tissues. Figure 2B shows a comparison of radioactivity uptake values for both nanotracers at 24 h p.i., whose target organs were the same. For both ^{89}Zr-AI-HDL (figure 2B, top) and ^{89}Zr-PL-HDL (figure 2B, bottom) kidneys were the main radioactivity accumulation site, however with marked quantitative differences. No statistically significant differences were found in tissue uptakes for ^{89}Zr-AI-HDL between diseased and control animals. However, when whole organ radioactivity accumulation was considered, uptake in kidneys, liver and spleen was significantly higher for atherosclerotic mice (figure S2A, top). For ^{89}Zr-PL-HDL, kidney and liver uptakes were significantly higher for control animals. At 48 h p.i. (figure S2B), kidneys were also the main activity accumulation site for both nanoparticles. For ^{89}Zr-AI-HDL, uptakes were as high as 80 %ID/g.

Micro-PET/CT imaging studies in mice

Non-invasive visualization of ^{89}Zr-HDL biodistribution in mice was investigated at 24 (figure 2C) and 48 h (figure S2B) after intravenous administration. For ^{89}Zr-AI-HDL, images were clearly dominated by strong signal from the kidneys, whereas for ^{89}Zr-PL-HDL liver and kidneys were the preferred accumulation sites. PET-derived uptake values were in good agreement with the *ex vivo* results (figure S2D).

Plaque targeting of ^{89}Zr-HDL nanoparticles in mice

Increased radioactivity accumulation in whole aortas of *Apoe*−/− mice was found for both NPs at 24 h. For ^{89}Zr-AI-HDL, the difference was significantly higher when only the aortic

root was considered (figure 3A, top). At 48 h a significantly higher accumulation in atherosclerotic aortas was found for ^{89}Zr-PL-HDL only (0.019 ± 0.04 %ID [n = 6] vs. 0.013 ± 0.03 %ID [n = 4] for controls, $P = 0.02$). In autoradiographic analysis, higher deposition of radioactivity was observed in atherosclerotic aortas (figure 3B), especially in aortic roots. Increased plaque accumulation of the fluorescent analogs of ^{89}Zr-HDL nanoparticles (DiR@Zr-AI-HDL and DiR@Zr-PL-HDL) was also observed in atherosclerotic aortas by NIRF imaging. Strong signals were observed originating from aortic roots of diseased animals at 24 (figure 3B) and 48 h p.i. Good correlations were found for both ^{89}Zr-AI-HDL ($\rho = 0.80$) and ^{89}Zr-PL-HDL ($\rho = 0.72$) between total radioactivity accumulation and total radiant efficiency of their fluorescent analogs at 24 h p.i. (figure 3C).

Pharmacokinetics and biodistribution of ^{89}Zr-HDL nanoparticles in rabbits

Similarly to the murine model, radioactivity clearance was slower for ^{89}Zr-AI-HDL (figure 4A, top), whose half-lives were 1.13 and 1.05 days in atherosclerotic and control animals, respectively. For ^{89}Zr-PL-HDL (figure 4A, bottom), clearance was slower in animals with atherosclerosis (0.44 vs. 0.34 days for controls). Radioactivity distribution in selected tissues was measured at 5 days p.i. (figure 4B). Kidneys showed the highest uptake values for both NPs, although they were 3–4-fold higher for ^{89}Zr-AI-HDL. Spleen and liver uptakes were around 0.1 %ID/g for the two NPs.

Imaging studies in rabbits

We evaluated our ^{89}Zr-HDL nanoparticles in rabbits by *in vivo* PET imaging on a clinical PET/CT scanner. Representative PET/CT fusion images of the abdominal region at three different time points can be seen in figure 4C for both nanoparticles. In addition, we also used a unique clinical PET/MRI system to investigate our nanoparticles' *in vivo* behavior in the same animals and time points for direct comparison. Figure 5A shows representative PET/MRI fusion images of the same animals shown in figure 4C. The PET images obtained with both scanners were almost identical (see supporting video). More importantly, there was a strong correlation between the SUVs measured from both systems (figures 5B) and also excellent agreement between the values, with an ICC of 0.99 (95% CI 0.98 – 0.99).

Time-activity curves based on data obtained from PET/CT and PET/MRI image analysis are shown in figures S3 to S6. Initially, within the first hour after intravenous administration, images were dominated by a strong blood pool signal for both ^{89}Zr-AI-HDL and ^{89}Zr-PL-HDL (figures 4C and 5A, 1 hour), as well as high signal from liver, spleen and kidneys. Blood radioactivity half-lives derived from PET/CT SUVs measured in the cardiac chambers were shorter than those obtained by blood sampling for both ^{89}Zr-AI-HDL (0.55 and 0.56 days for animals with atherosclerosis and controls, respectively) and ^{89}Zr-PL-HDL (0.27 and 0.31 days for diseased animals and controls, respectively). At later time points, ^{89}Zr-AI-HDL images showed very high radioactivity accumulation in kidneys, which was significantly higher in atherosclerotic animals at all time points investigated (figure S3A and S4A). For ^{89}Zr-PL-HDL, strong gall bladder signals (GB, figure 4C bottom; SUVs as high as 20 g/mL) were observed at 1 and 2 days p.i., which was accompanied by high radioactivity accumulation in the stomach and intestines. Intense signals from the kidneys were also observed at all time points for ^{89}Zr-PL-HDL. In both cases, bone radioactivity

accumulation was also detected over the five-day period (SUVs around 5 g/mL). *Ex vivo* analysis proved that this was mostly due to bone marrow uptake, as opposed to mineral bone. Bone marrow uptake was higher in animals with atherosclerosis for ^{89}Zr-AI-HDL (0.17 ± 0.03 vs. 0.13 ± 0.01 %ID/g for controls) while for ^{89}Zr-PL-HDL values were similar (0.039 ± 0.010 and 0.050 ± 0.002 %ID/g for rabbits with atherosclerosis and controls, respectively). PET-measured SUVs were in good agreement with SUVs determined by *ex vivo* gamma counting (figure S7), although they were typically lower.

Increased aortic radioactivity accumulation was found at day 5 p.i. for both probes in atherosclerotic aortas compared to controls by PET/CT imaging (figure 6A). The difference was statistically significant for ^{89}Zr-PL-HDL ($P = 0.03$). For ^{89}Zr-AI-HDL at 1, 2 and 3 days p.i. the high blood pool signal dominated the measurements, as evidenced by the similar blood and aorta ratios between SUVs in atherosclerotic and control rabbits (figure S8A, top). We found a very similar increased accumulation in atherosclerotic aortas for either ^{89}Zr-AI-HDL (0.40 ± 0.08 vs. 0.34 ± 0.10 g/mL) or ^{89}Zr-PL-HDL (0.24 ± 0.13 vs. 0.15 ± 0.08 g/mL) at 5 days p.i using PET/MRI. At earlier time points, values were very similar for both NPs in animals with atherosclerosis and controls.

Plaque targeting of ^{89}Zr-HDL nanoparticles in rabbits

Radioactivity concentration was significantly higher in atherosclerotic aortas for both ^{89}Zr-AI-HDL ($P = 0.03$) and ^{89}Zr-PL-HDL ($P = 0.03$) as determined by gamma counting at 5 days p.i. (figure 6A). Autoradiography of explanted aortas revealed a patchy distribution of radioactivity in atherosclerotic aortas, showing preferential accumulation in lesions (figure 6B). Analysis by NIRF imaging showed increased accumulation of Cy5.5-HDL in atherosclerotic aortas (figure 6B). A good correlation was found between total radiant efficiency and radioactivity concentration (figures 6C and S8B). Interestingly, correlation between radioactivity concentration and Cy7-albumin NIRF intensity was weak (figure S8C), suggesting permeability may not be an HDL accumulation determinant.

Oxidized HDL imaging experiments in atherosclerotic rabbits

Blood radioactivity clearance for radiolabeled ^{89}Zr-AI-HDL^{Ox} nanoparticles was significantly faster than for ^{89}Zr-AI-HDL in both animals with atherosclerosis and controls (figure S9A), and its half-life was 3 times as short ($t_{1/2} = 0.33$ days). Radioactivity distribution, however, showed a similar pattern at day 5 p.i (figure S9B). ^{89}Zr-AI-HDL^{Ox} uptake values were significantly lower in liver and lungs compared to ^{89}Zr-AI-HDL in both atherosclerotic and control animals, and in spleen compared to ^{89}Zr-AI-HDL in diseased animals. PET/CT (figure S9C) and PET/MR images showed very high accumulation in kidneys at all time points, with SUVs as high as 48 g/mL (1.0 %ID/g). These values were significantly higher than those measured for ^{89}Zr-AI-HDL in controls and rabbits with atherosclerosis (figure S7D). PET-quantified SUVs were qualitatively similar to the values obtained after the 5th day scan by *ex vivo* gamma counting (figure S9D). Interestingly, radioactivity accumulation in atherosclerotic aortas for ^{89}Zr-AI-HDL^{Ox} was significantly lower than for non-oxidized ^{89}Zr-AI-HDL (figure S9E).

Imaging studies in pigs

Three pigs were imaged at 48 h after administration of ^{89}Zr-PL-HDL. A whole-body PET maximum intensity projection image obtained on the clinical PET/CT scanner can be seen in figure 7A. Strong signals were observed in kidneys, liver and bone, as well as in the intestines. High radioactivity accumulation in the femoral arteries could be clearly observed *in vivo* (figure 7B). Radioactivity concentration in these vessels was higher than in non-injured internal iliac arteries, which served as controls (figure 7B). Radioactivity distribution in selected organs determined by gamma counting after the 48 h scan is shown in figure 7C, and mirrors the PET imaging observations. The increased signal in the femoral arteries was due to accumulation in lesions, as corroborated by *ex vivo* autoradiography analysis (figure 7D).

DISCUSSION

In this study, we developed and validated a non-invasive quantifiable PET imaging tool to study HDL's *in vivo* behavior in multiple atherosclerosis models. Using non-radioactive fluorescent analogs of the ^{89}Zr-labeled nanoparticles we found that both preferentially targeted macrophages in the atherosclerotic aortas of *Apoe*$^{-/-}$ mice, in line with our previous studies (17)(18). This also suggests that the modifications were well tolerated and did not affect HDL's ability to interact with plaque macrophages (19).

Radioactivity clearance followed similar patterns in both mice and rabbits, showing longer half-lives for ^{89}Zr-AI-HDL (apolipoprotein-labeled) in healthy controls and for ^{89}Zr-PL-HDL (phospholipid-labeled) in atherosclerotic animals. ^{89}Zr-AI-HDL's longer half-life compared to ^{89}Zr-PL-HDL in control animals may be explained by the low net internalization rate and recycling of the protein (20). On the other hand, the slower clearance of ^{89}Zr-PL-HDL in animals with atherosclerosis, especially in the *Apoe*$^{-/-}$ mouse model, may be due to the elevated lipoprotein blood pool concentration and impaired lipid metabolism and clearance.

Modification of APOA1 can affect its blood circulation time as reported for radioiodination (21), which has been frequently used to study the pharmacokinetics and metabolism of the protein and of HDL (22). This is a very convenient labeling strategy that results in iodination of tyrosine residues but also in faster clearance than the unmodified protein (28), which is most likely due to rapid deiodination by deiodinases (23). Therefore, label stability and kinetics play an important role when designing an imaging tool. Importantly, using our approach, the radioactivity blood half-life of ^{89}Zr-AI-HDL in rabbits is in close agreement with values obtained by radioimmunometric assays using unmodified human APOA1 in the same animal (21), implying that the modifications to incorporate the ^{89}Zr label were well tolerated. Previously reported data do not show this strong corroboration between ^{125}I-labeled HDL, i.e. ^{125}I-HDL/^{125}I-APOA1, and unmodified HDL, which underestimates the actual blood half-life by a factor of 7–8 (21).

Our imaging studies show the same patterns in radioactivity distribution for the three animal models used, the kidneys being a main site of accumulation for both ^{89}Zr-AI-HDL and ^{89}Zr-PL-HDL (figure S10). It is well established that the kidney is a major catabolism site for

APOA1 and certain HDL subclasses (24)(25)(26). Quantitative analysis revealed a significantly higher kidney uptake in atherosclerotic rabbits at all time points for ^{89}Zr-AI-HDL. The SUVs showed little variation over time, suggesting a steady state situation. More importantly, the higher kidney uptakes found for ^{89}Zr-AI-HDL in rabbits with atherosclerosis were accompanied by lower blood radioactivity concentrations and, indeed, higher glomerular filtration rate has been related to lower HDL and APOA1 blood levels in humans without kidney disease (27) and to subclinical cardiovascular disease in non-diabetic subjects (28).

While ^{89}Zr-AI-HDL shows very high uptake in the kidneys, the radioactivity for ^{89}Zr-PL-HDL is more evenly distributed between kidneys, liver and spleen and, at later time points, the digestive system. Initially, very high uptakes were found in the gall bladder (both for controls and animals with atherosclerosis), suggesting incorporation of the radiolabeled phospholipid to the bile and subsequent excretion. The detection of radioactivity in the stomach can be explained by the presence of the radioactive compound in the *caecotrophs* (nutritious stools resulting from gut bacteria digestion) that rabbits selectively ingest (29).

Ex vivo analysis of rabbit bone samples revealed that most of this uptake originated from the bone marrow and that, for ^{89}Zr-AI-HDL, this uptake was higher in animals with atherosclerosis. This may reflect the interaction of ^{89}Zr-HDL nanoparticles with hematopoietic stem and multipotent progenitor cells, which overexpress the ABCG1 transporter involved in HDL-mediated cholesterol efflux (30).

Interestingly, blood radioactivity clearance for oxidized HDL nanoparticles (^{89}Zr-AI-HDL^{Ox}) in atherosclerotic animals was significantly faster than its unoxidized counterpart in both control and diseased animals and was paralleled by a significantly increased kidney radioactivity accumulation. The shorter blood half-life of ^{89}Zr-AI-HDL^{Ox} is probably the main reason why its accumulation in the plaque is significantly decreased when compared to non-oxidized ^{89}Zr-AI-HDL, but impaired interaction with its receptors could also be partly responsible. These results are in agreement with a recent study using myeloperoxidase-oxidized APOA1 (31).

As a proof of principle, we tested one of our ^{89}Zr-labeled nanoparticles, namely ^{89}Zr-PL-HDL, in a porcine model of atherosclerosis. The target organs were the same (mainly kidneys and liver) with comparable SUVs to those observed in the rabbit studies. Atherosclerotic lesions were clearly visible at 48 h post administration despite the blood pool signal, suggesting that vessel wall inflammation can be imaged by HDL-PET in severe cases.

In addition to PET/CT, in the rabbit model we also performed extensive PET/MRI studies. Importantly, the PET/MRI data were in excellent agreement with the PET/CT data. Integrative PET/MRI has only recently become available (32) and allows direct vessel (morphology) visualization, without administration of an additional agent to delineate the vasculature. To the best of our knowledge, this is the first time PET/MRI has been applied to monitor nanoparticle accumulation in the atherosclerotic vessel wall.

CONCLUSIONS

In summary, ^{89}Zr labeling allows studying HDL's *in vivo* behavior by PET combined with CT or MRI. This imaging tool allows the non-invasive evaluation of HDL's and could be of great value to study its metabolism and trafficking in preclinical and clinical settings. Ultimately, in the context of advanced clinical atherosclerosis, this non-invasive imaging tool is ideal to identify patients amenable to HDL therapy and subsequent treatment monitoring in a theranostic fashion.

Supplementary Material

Refer to Web version on PubMed Central for supplementary material.

Acknowledgments

The authors thank the Small Animal Imaging Core and the Radiochemistry and Molecular Imaging Probes Core at Memorial Sloan Kettering Cancer Center for their assistance. The authors thank the NIH for funding through the Program of Excellence in Nanotechnology (PEN) Award (HHSN368201000045C, to Z.A.F), and through grants R01 EB009638 (Z.A.F.), R01 HL118440 (W.J.M.M.), R01 HL125703 (W.J.M.M.), R01 CA155432 (W.J.M.M.), NWO Vidi 91713324 (W.J.M.M.), and CNIC for the CardioImage program (C.P.M.).

Abbreviations list

APOA1	Apolipoprotein A-I
DFO	Deferoxamine B
DMPC	1,2-dimyristoyl-sn-glycero-3-phosphocholine
DSPE	1,2-distearoyl-sn-glycero-3-phosphoethanolamine
HDL	High-density lipoprotein
HFD	High-fat diet
%ID/g	Percentage injected dose per gram
NIRF	Near infrared fluorescence
NP	Nanoparticle
p.i.	post injection
ROI	Region of interest
SUV	Standardized uptake value

REFERENCES

1. Lusis AJ. Atherosclerosis. Nature. 2000; 407:233–241. [PubMed: 11001066]
2. Libby P. Inflammation in atherosclerosis. Nature. 420:868–874.
3. Libby P, Ridker PM, Hansson GK. Progress and challenges in translating the biology of atherosclerosis. Nature. 2011; 473:317–325. [PubMed: 21593864]

4. Fuster V, Moreno PR, Fayad ZA, Corti R, Badimon JJ. Atherothrombosis and high-risk plaque: part I: evolving concepts. J. Am. Coll. Cardiol. 2005; 46:937–954. [PubMed: 16168274]
5. Favari E, Chroni A, Tietge UJF, Zanotti I, Escolà-Gil JC, Bernini F. Cholesterol efflux and reverse cholesterol transport. Handb. Exp. Pharmacol. 2015; 224:181–206. [PubMed: 25522988]
6. Badimon JJ, Badimon L, Fuster V. Regression of atherosclerotic lesions by high density lipoprotein plasma fraction in the cholesterol-fed rabbit. J. Clin. Invest. 1990; 85:1234–1241. [PubMed: 2318976]
7. Rubin EM, Krauss RM, Spangler EA, Verstuyft JG, Clift SM. Inhibition of early atherogenesis in transgenic mice by human apolipoprotein AI. Nature. 1991; 353:265–267. [PubMed: 1910153]
8. Tardif J-C, Grégoire J, L'Allier PL, et al. Effects of reconstituted high-density lipoprotein infusions on coronary atherosclerosis: a randomized controlled trial. JAMA. 2007; 297:1675–1682. [PubMed: 17387133]
9. Rader DJ, Daugherty A. Translating molecular discoveries into new therapies for atherosclerosis. Nature. 2008; 451:904–913. [PubMed: 18288179]
10. Van Eck M, Pennings M, Hoekstra M, Out R, Van Berkel TJ. Scavenger receptor BI and ATP-binding cassette transporter A1 in reverse cholesterol transport and atherosclerosis. Curr. Opin. Lipidol. 2005; 16:307–315. [PubMed: 15891392]
11. Yvan-Charvet L, Wang N, Tall AR. Role of HDL, ABCA1, and ABCG1 transporters in cholesterol efflux and immune responses. Arterioscler. Thromb. Vasc. Biol. 2010; 30:139–143. [PubMed: 19797709]
12. Frias JC, Williams KJ, Fisher E, Fayad Z. Recombinant HDL-like nanoparticles: A specific contrast agent for MRI of atherosclerotic plaques. J. Am. Chem. Soc. 2004; 126:16316–16317. [PubMed: 15600321]
13. Cormode DP, Chandrasekar R, Delshad A, et al. Comparison of synthetic high density lipoprotein (HDL) contrast agents for MR imaging of atherosclerosis. Bioconjug. Chem. 2009; 20:937–943. [PubMed: 19378935]
14. Bulte JWM. Hot spot MRI emerges from the background. Nat. Biotechnol. 2005; 23:945–946. [PubMed: 16082363]
15. Pérez-Medina C, Abdel-Atti D, Zhang Y, et al. A Modular Labeling Strategy for In Vivo PET and Near-Infrared Fluorescence Imaging of Nanoparticle Tumor Targeting. J. Nucl. Med. 2014; 55:1706–1712. [PubMed: 25060196]
16. Pérez-Medina C, Tang J, Abdel-Atti D, et al. PET Imaging of Tumor-Associated Macrophages with 89Zr-labeled HDL Nanoparticles. J. Nucl. Med. 2015; 56:1272–1277. [PubMed: 26112022]
17. Duivenvoorden R, Tang J, Cormode DP, et al. A statin-loaded reconstituted high-density lipoprotein nanoparticle inhibits atherosclerotic plaque inflammation. Nat. Commun. 2014; 5:3065. [PubMed: 24445279]
18. Tang J, Lobatto ME, Hassing L, et al. Inhibiting macrophage proliferation suppresses atherosclerotic plaque inflammation. Sci. Adv. 2015; 1:e1400223–e1400223. [PubMed: 26295063]
19. Westerterp M, Bochem AE, Yvan-Charvet L, Murphy AJ, Wang N, Tall AR. ATP-binding cassette transporters, atherosclerosis, and inflammation. Circ. Res. 2014; 114:157–170. [PubMed: 24385509]
20. Röhrl C, Stangl H. HDL endocytosis and resecretion. Biochim. Biophys. Acta. 2013; 1831:1626–1633. [PubMed: 23939397]
21. Braschi S, Neville TA-M, Maugeais C, Ramsamy TA, Seymour R, Sparks DL. Role of the Kidney in Regulating the Metabolism of HDL in Rabbits: Evidence That Iodination Alters the Catabolism of Apolipoprotein A-I by the Kidney. Biochemistry. 2000; 39:5441–5449. [PubMed: 10820016]
22. Shaish A, Keren G, Chouraqui P, Levkovitz H, Harats D. Imaging of aortic atherosclerotic lesions by 125I-LDL, 125I-oxidized-LDL, 125I-HDL and 125I-BSA. Pathobiology. 2001; 69:225–229. [PubMed: 12007282]
23. Zalutsky MR, Narula AS. A method for the radiohalogenation of proteins resulting in decreased thyroid uptake of radioiodine. Int. J. Radiat. Appl. Instrumentation. Part A. Appl. Radiat. Isot. 1987; 38:1051–1055.
24. Glass CK, Pittman RC, Keller GA, Steinberg D. Tissue sites of degradation of apoprotein A-I in the rat. J. Biol. Chem. 1983; 258:7161–7167. [PubMed: 6406495]

25. Moestrup SK, Nielsen LB. The role of the kidney in lipid metabolism. Curr. Opin. Lipidol. 2005; 16:301–306. [PubMed: 15891391]
26. Breznan D, Veereswaran V, Viau FJ, Neville TA-M, Sparks DL. The lipid composition of high-density lipoprotein affects its re-absorption in the kidney by proximal tubule epithelial cells. Biochem. J. 2004; 379:343–349. [PubMed: 14711371]
27. Krikken JA, Gansevoort RT, Dullaart RPF. Lower HDL-C and apolipoprotein A-I are related to higher glomerular filtration rate in subjects without kidney disease. J. Lipid Res. 2010; 51:1982–1990. [PubMed: 20211930]
28. Eriksen BO, Løchen M-L, Arntzen KA, et al. Subclinical cardiovascular disease is associated with a high glomerular filtration rate in the nondiabetic general population. Kidney Int. 2014; 86:146–153. [PubMed: 24304885]
29. Hirakawa H. Coprophagy in leporids and other mammalian herbivores. Mamm. Rev. 2001; 31:61–80.
30. Yvan-Charvet L, Pagler T, Gautier EL, et al. ATP-binding cassette transporters and HDL suppress hematopoietic stem cell proliferation. Science. 2010; 328:1689–1693. [PubMed: 20488992]
31. Hewing B, Parathath S, Barrett T, et al. Effects of native and myeloperoxidase-modified apolipoprotein a-I on reverse cholesterol transport and atherosclerosis in mice. Arterioscler Thromb Vasc Biol. 2014; 34:779–789. [PubMed: 24407029]
32. Sauter AW, Wehrl HF, Kolb A, Judenhofer MS, Pichler BJ. Combined PET/MRI: one step further in multimodality imaging. Trends Mol. Med. 2010; 16:508–515. [PubMed: 20851684]

Clinical Perspectives

Competency in Medical Knowledge

High-density lipoprotein (HDL) labeled with the long-lived radioisotope 89Zr is a novel tracer to study its pharmacokinetics and biodistribution with in vivo PET imaging. Our PET imaging technology can help to elucidate certain aspects of HDL's function under physiological and pathophysiological conditions.

Translational Outlook

HDL-cholesterol is a strong predictor of cardiovascular risk. As such, pharmaceutical companies are exploring its use as an injectable therapeutic. Using the presented imaging approach, HDL’s organ and atherosclerotic plaque accumulation kinetics can be quantitatively studied, in a noninvasive fashion, and help to identify patients that are amenable to HDL therapy.

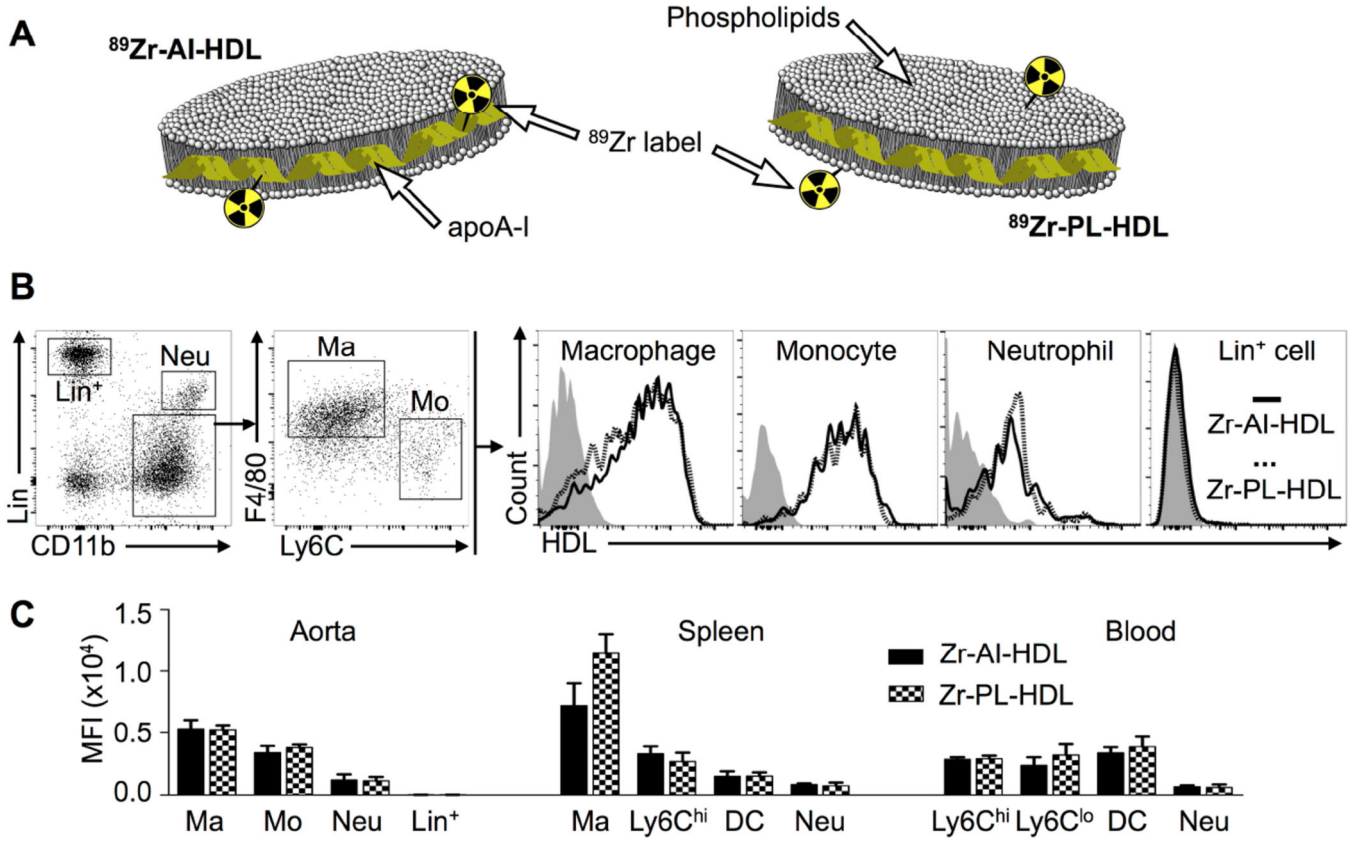

Figure 1. ^{89}Zr-HDL nanoparticles and their cellular targets in a mouse atherosclerosis model

A) Schematic of ^{89}Zr-APOA1-labeled HDL (^{89}Zr-AI-HDL) and ^{89}Zr-phospholipid-labeled HDL (^{89}Zr-PL-HDL). B) Gating procedure and cell targets of Zr-HDL nanoparticles in mouse atherosclerotic aortas. Non-radioactive fluorescent DiR-labeled analogs were used to determine cell-targeting preference in the aortas of *Apoe*$^{-/-}$ mice (18 weeks on HFD) by flow cytometry. C) Quantification of DiR concentration as mean fluorescence intensity (MFI) in different cell types in the aorta, spleen and blood of *Apoe*$^{-/-}$ mice (18 weeks on HFD).

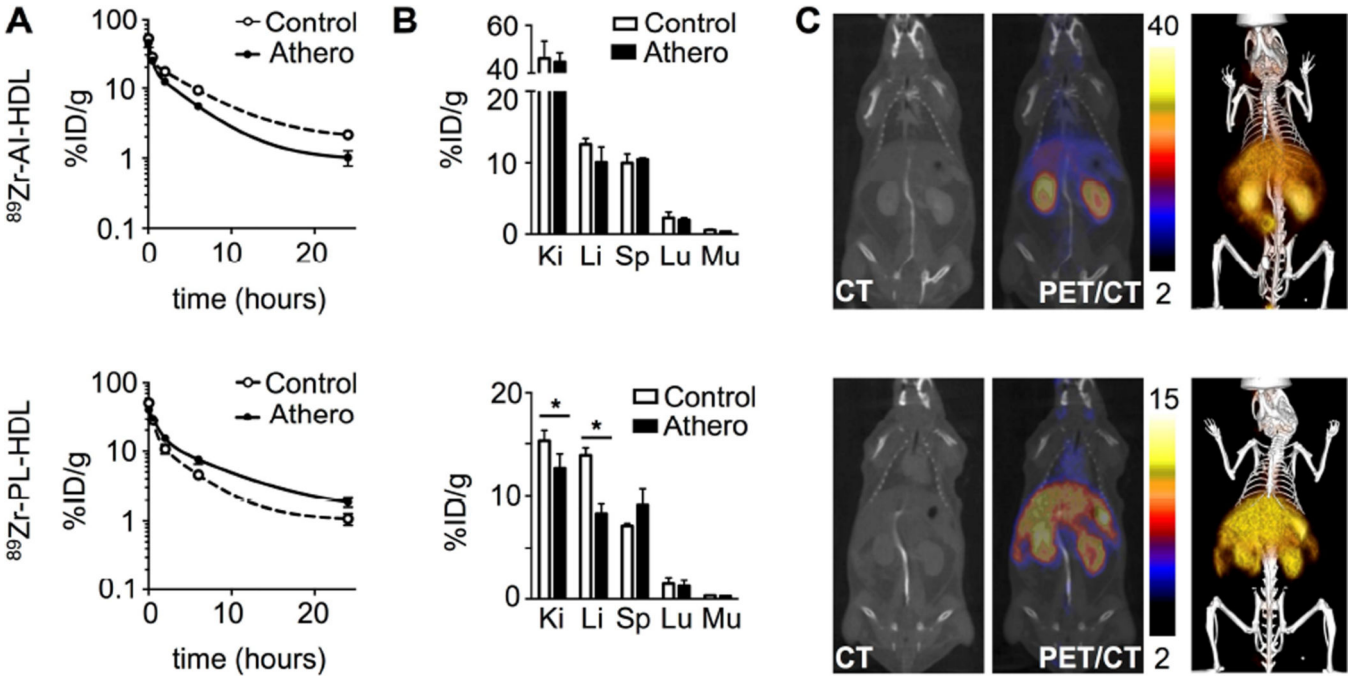

Figure 2. ^{89}Zr-HDL pharmacokinetics and PET/CT imaging in mice

A) Blood time-activity curves for ^{89}Zr-AI-HDL (top) and ^{89}Zr-PL-HDL (bottom) in *Apoe*$^{-/-}$ (18 weeks on HFD) and wild type B6 mice (n = 3 per group). B) Radioactivity distribution in selected tissues for ^{89}Zr-AI-HDL (top) and ^{89}Zr-PL-HDL (bottom) at 24 h p.i. [Ki: kidney; Li: liver; Sp: spleen; Lu: lungs; Mu: muscle] (n ≥ 4 per group). C) PET/CT imaging of ^{89}Zr-AI-HDL (top) and ^{89}Zr-PL-HDL (bottom) at 24 h p.i in *Apoe*$^{-/-}$ (18 weeks on HFD), showing CT only (left), PET/CT fusion images (middle; scale bar indicates %ID/g) and 3D-rendering PET/CT fusion image (right). * $P < 0.05$.

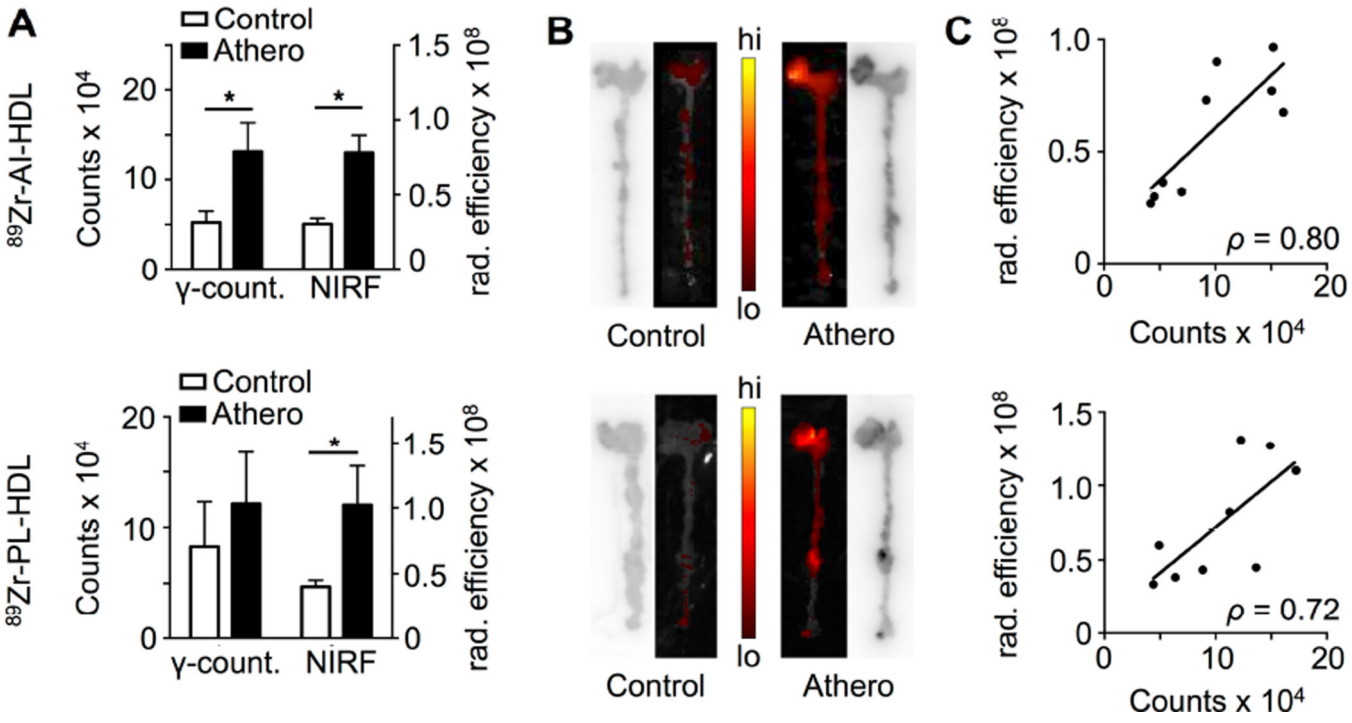

Figure 3. Plaque targeting of ^{89}Zr-HDL nanoparticles in *Apoe*−/− mice

A) Comparison between radioactivity content and NIRF intensity (total radiant efficiency, in μW/cm^2) in the aortic roots of *Apoe*$^{-/-}$ (18 weeks on HFD) and wild type B6 mice at 24 h p.i. of ^{89}Zr-AI-HDL and DiR@Zr-AI-HDL (top) and ^{89}Zr-PL-HDL and DiR@Zr-PL-HDL (bottom) (n ≥ 4 per group). B) Autoradiography and NIRF images of whole aortas of *Apoe*$^{-/-}$ (18 weeks on HFD) and wild type B6 mice at 24 h p.i. of ^{89}Zr-AI-HDL and DiR@Zr-AI-HDL (top) and ^{89}Zr-PL-HDL and DiR@Zr-PL-HDL (bottom). C) Correlation between radioactivity content and NIRF intensity (total radiant efficiency, in μW/cm^2) in the aortic roots of *Apoe*$^{-/-}$ (18 weeks on HFD) and wild type B6 mice at 24 h p.i. of ^{89}Zr-AI-HDL and DiR@Zr-AI-HDL (top) and ^{89}Zr-PL-HDL and DiR@Zr-PL-HDL (bottom) (n ≥ 4 per group). * $P < 0.05$.

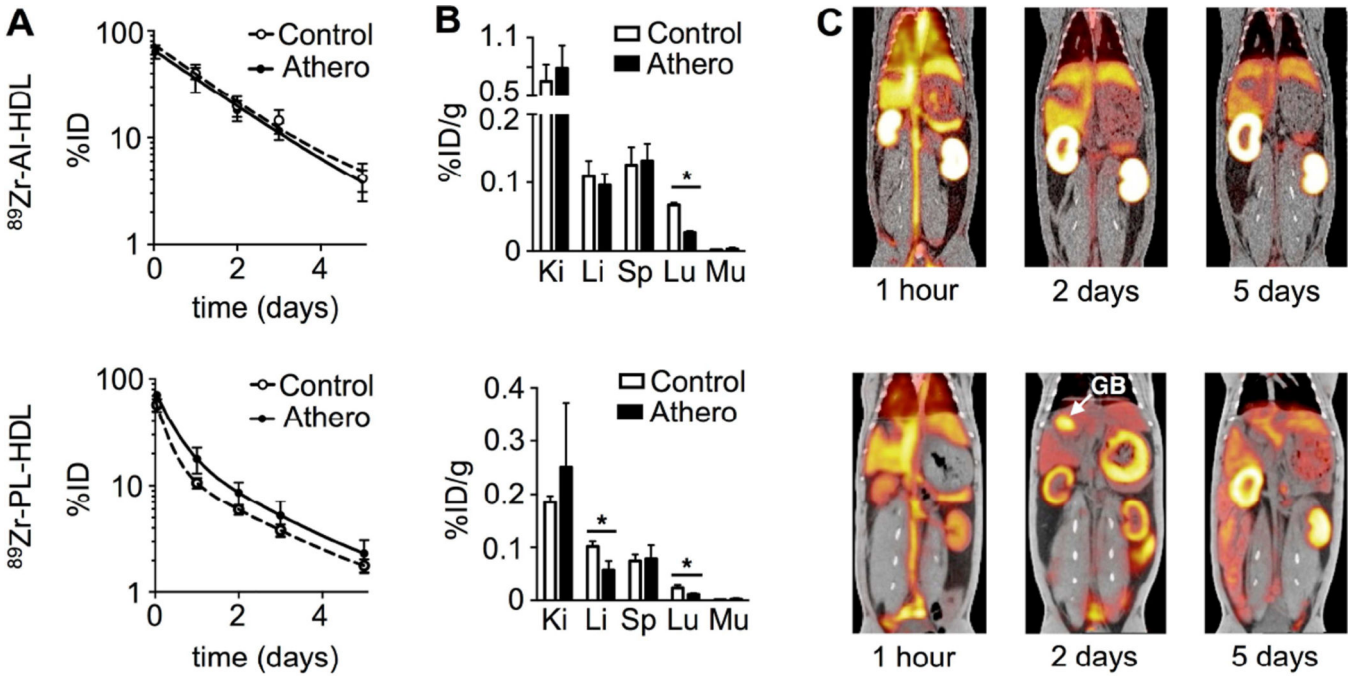

Figure 4. ^{89}Zr-HDL pharmacokinetics and PET/CT imaging in rabbits

A) Blood time-activity curves for ^{89}Zr-AI-HDL (top) and ^{89}Zr-PL-HDL (bottom) in rabbits with atherosclerosis and wild type controls (n = 4 per group). B) Radioactivity distribution in selected tissues for ^{89}Zr-AI-HDL (top) and ^{89}Zr-PL-HDL (bottom) at 5 days p.i. [Ki: kidney; Li: liver; Sp: spleen; Lu: lungs; Mu: muscle] (n = 4 per group). C) PET/CT fusion images of ^{89}Zr-AI-HDL (top) and ^{89}Zr-PL-HDL (bottom) at 1 h, 2 and 5 days p.i. in rabbits with atherosclerosis (GB: gall bladder). * $P < 0.05$.

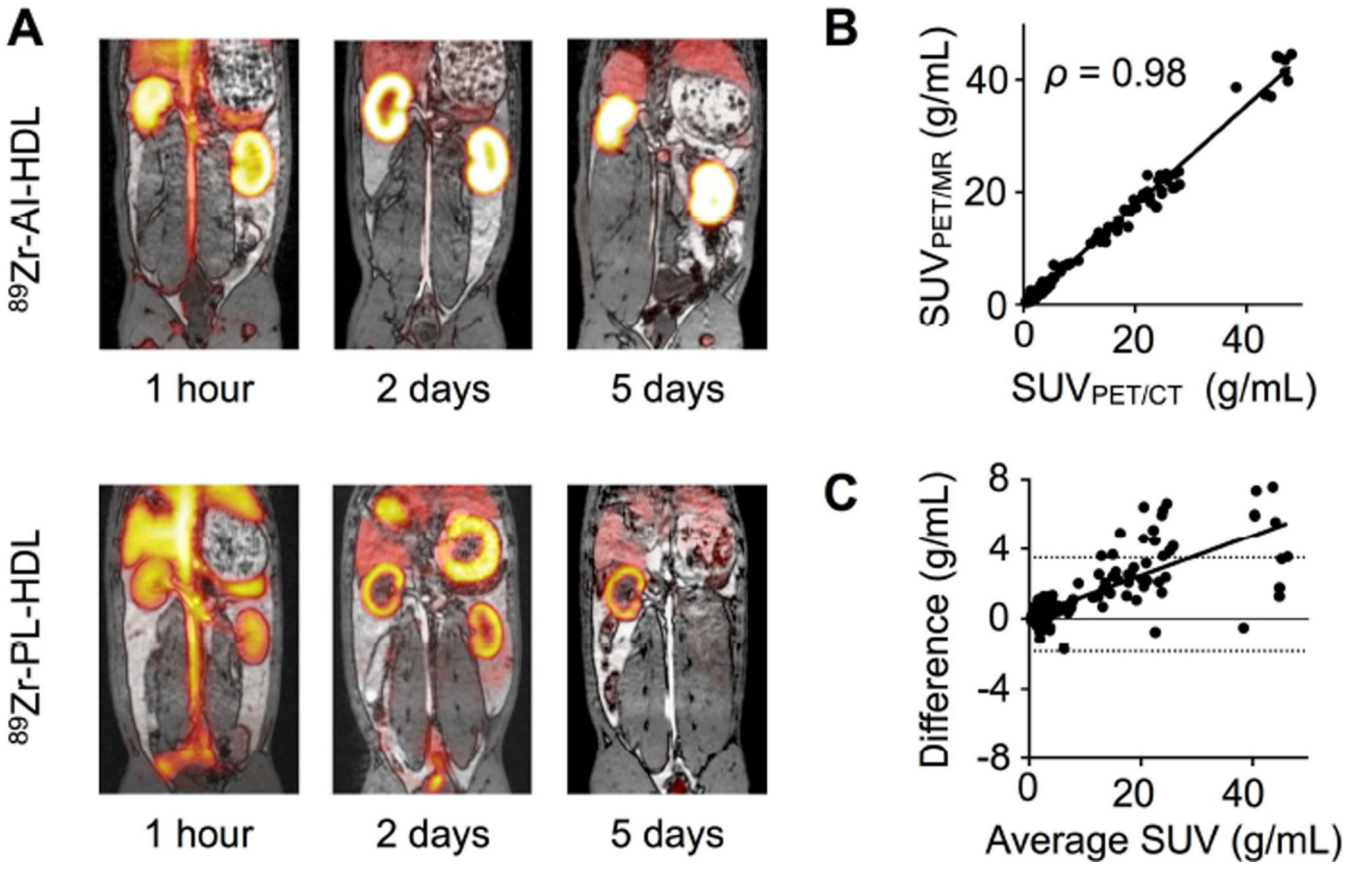

Figure 5. PET/MRI imaging of ^{89}Zr-HDL in rabbits

A) PET/MRI fusion images of ^{89}Zr-AI-HDL (top) and ^{89}Zr-PL-HDL (bottom) at 1 h, 2 and 5 days p.i. in rabbits with atherosclerosis. B) Correlation between SUVs determined by PET/MRI and PET/CT imaging for the same tissue and time point (n = 295). C) Bland-Altman plot of the difference ($SUV_{PET/CT}$ - $SUV_{PET/MRI}$) and average SUVs obtained from the PET/CT and PET/MRI systems for the same tissue and time point (n = 295).

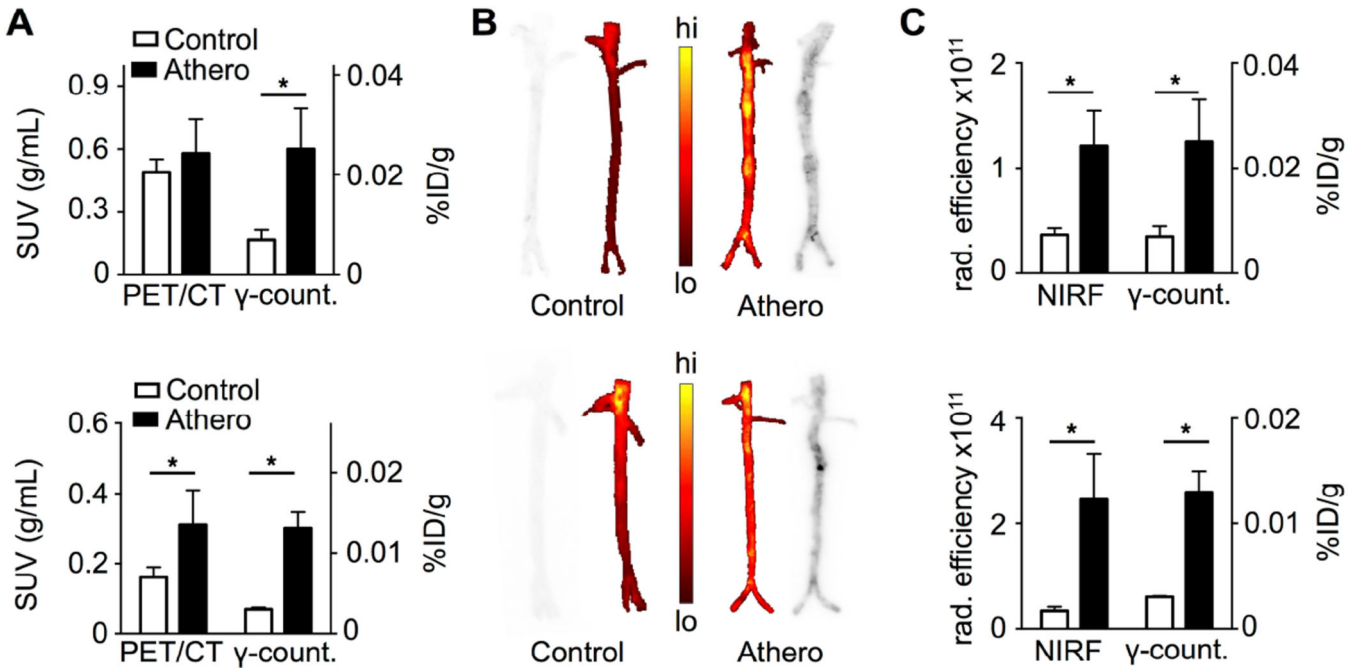

Figure 6. Plaque targeting of ^{89}Zr-HDL nanoparticles in rabbits with atherosclerosis

A) Comparison between SUVs measured from PET/CT images and radioactivity concentration in aortas of rabbits with atherosclerosis and wild type controls at 5 days p.i. of ^{89}Zr-AI-HDL (top) and ^{89}Zr-PL-HDL (bottom) (n = 4 per group). B) Autoradiography and NIRF images of whole aortas from rabbits with atherosclerosis and wild type controls at 5 days post administration of ^{89}Zr-AI-HDL and Cy5.5-HDL (top) and ^{89}Zr-PL-HDL and Cy5.5-HDL (bottom). C) Comparison between NIRF intensity (total radiant efficiency, in μW/cm^2) and radioactivity concentration in aortas of rabbits with atherosclerosis and wild type controls at 5 days post administration of ^{89}Zr-AI-HDL and Cy5.5-HDL (top) and ^{89}Zr-PL-HDL and Cy5.5-HDL (bottom) (n = 4 per group). * $P < 0.05$.

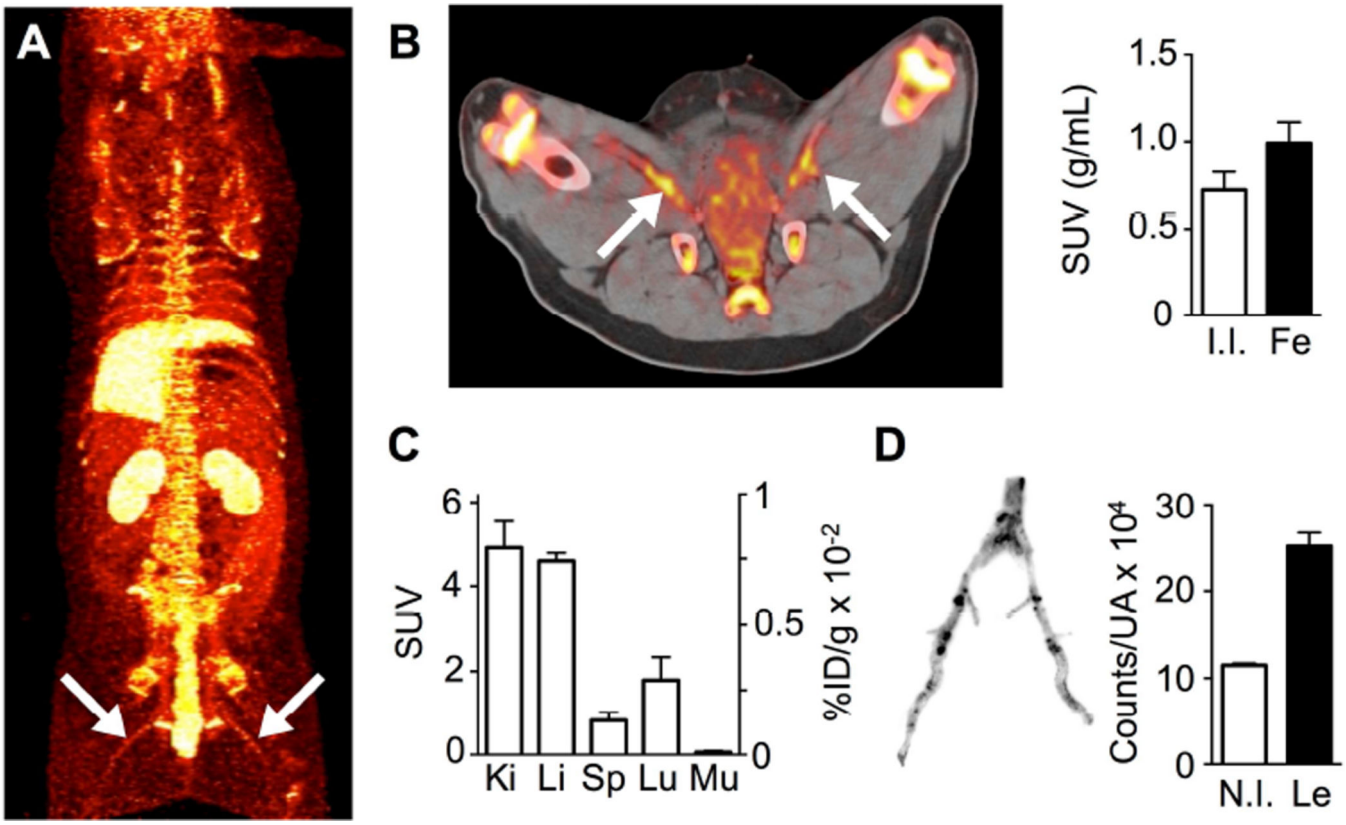

Figure 7. PET imaging and plaque targeting of ^{89}Zr-PL-HDL in a porcine model of atherosclerosis

A) Whole-body maximum intensity projection PET image of a pig injected with ^{89}Zr-PL-HDL at 48 h p.i. (arrows indicating lesions). B) Axial PET/CT image showing high radioactivity accumulation in lesions -indicated by arrows- at 48 h p.i. (left), and quantification of radioactivity concentrations (right) in internal iliac (I.I., chosen as control) and femoral arteries (Fe)(n = 3). C) Radioactivity distribution in selected tissues for ^{89}Zr-PL-HDL at 48 h p.i. determined by gamma counting (n = 3). D) Autoradiography of femoral arteries (left) and quantification of radioactivity concentration (counts per unit area) in non-injured tissue (N.I.) and lesions (Le) determined from the autoradiographies (right)(n = 3).